Robot-assisted spidermass for in vivo real-time topography mass spectrometry imaging

Nina Ogrinc, Alexandre Kruszewski, Paul Chaillou, Philippe Saudemont, Chann Lagadec, Michel Salzet, Christian Duriez, Isabelle Fournier

analytical chemistry

pubs.acs.org/ac Article

Robot-Assisted SpiderMass for *In Vivo* Real-Time Topography Mass Spectrometry Imaging

Nina Ogrinc, Alexandre Kruszewski, Paul Chaillou, Philippe Saudemont, Chann Lagadec, Michel Salzet, Christian Duriez,* and Isabelle Fournier*

Cite This: *Anal. Chem.* 2021, 93, 14383−14391 Read Online

ACCESS | Metrics & More | Article Recommendations | Supporting Information

ABSTRACT: Mass spectrometry imaging (MSI) has shown to bring invaluable information for biological and clinical applications. However, conventional MSI is generally performed *ex vivo* from tissue sections. Here, we developed a novel MS-based method for *in vivo* mass spectrometry imaging. By coupling the SpiderMass technology, that provides *in vivo* minimally invasive analysis—to a robotic arm of high accuracy, we demonstrate that images can be acquired from any surface by moving the laser probe above the surface. By equipping the robotic arm with a sensor, we are also able to both get the topography image of the sample surface and the molecular distribution, and then and plot back the molecular data, directly to the 3D topographical image without the need for image fusion. This is shown for the first time with the 3D topographic MS-based whole-body imaging of a mouse. Enabling fast *in vivo* MSI bridged to topography paves the way for surgical applications to excision margins.

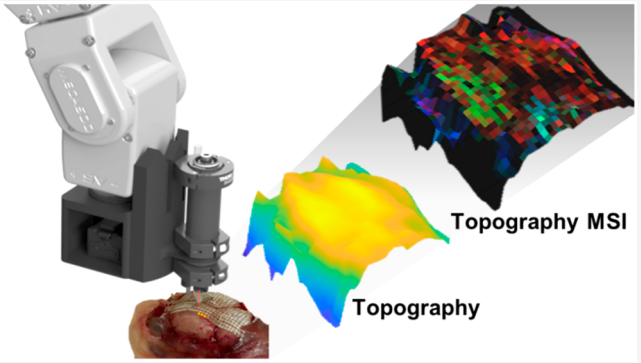

Mass spectrometry (MS) has, over the past two decades, moved closer to the patient's bedside. Particularly, the development of mass spectrometry imaging (MSI), first with matrix-assisted laser desorption ionization (MALDI-MSI) and later with desorption electrospray ionization (DESI-MSI), has spurred interest for molecular imaging in oncology.[1−3] The technology has demonstrated that collected MS molecular profiles are specific to cell phenotypes and provide access to the molecular content in the tumor microenvironment. On the other hand, the introduction of MS directly in the surgical theater represented a true paradigm shift by transforming MS from a lab technology into a clinical tool. Several intraoperative MS techniques, either for *ex vivo* tissue analysis on the bench, or directly targeting *in vivo*, have been developed. With respect to *in vivo*, a few different MS techniques based on direct coupling to either surgical,[4−6] laser[7−9] or liquid extraction devices[10] have revolutionized the surgico-clinical field. These *in vivo* techniques target the same goal by helping practitioners with decision making during surgery. To date *in vivo* MS has only been demonstrated by manual analysis of defined spots on the tissue, and for classification purposes of molecular profiles.

However, to provide the global "picture" to the surgeon and improve the decision-making process, a complete area needs to be imaged by an autonomous system. To achieve *in vivo* MS imaging several constraints, need to be taken into consideration including that (i) the sample cannot be moved under the analytical beam and (ii) the biological tissue must not be altered in any way. Indeed, conventional MSI is realized from flat samples surfaces with the sample probe moving under the analytical beam. Some instruments such as the TOF-SIMS and a few MALDI systems offer the possibility to electrostatically move the analytical beam at the scale of the field view but only for a very limited area (<0.1 mm^2). A way to conduct *in vivo* imaging is to develop a system where the analytical beam is moving in a well-controlled fashion in three dimensions with enough accuracy above the sample surface to address the analysis of the surfaces from tissues in 3D.

Here, we introduce topography molecular imaging by robotically assisted MSI as a novel way to achieve *in vivo* imaging. The topography MSI is designed to image raw samples in real-time while providing both the topography and the related molecular information. We developed a robotic arm system coupled to the water-assisted laser desorption ionization technology (SpiderMass). SpiderMass is an emerging mini-invasive IR laser-based MS technique designed for *in vivo* real-time molecular analysis[7,8] and has been showcased at the veterinary surgery room for tissue profiling.[11] The method is based on the resonant excitation of the

Received: April 21, 2021
Accepted: September 28, 2021
Published: October 20, 2021

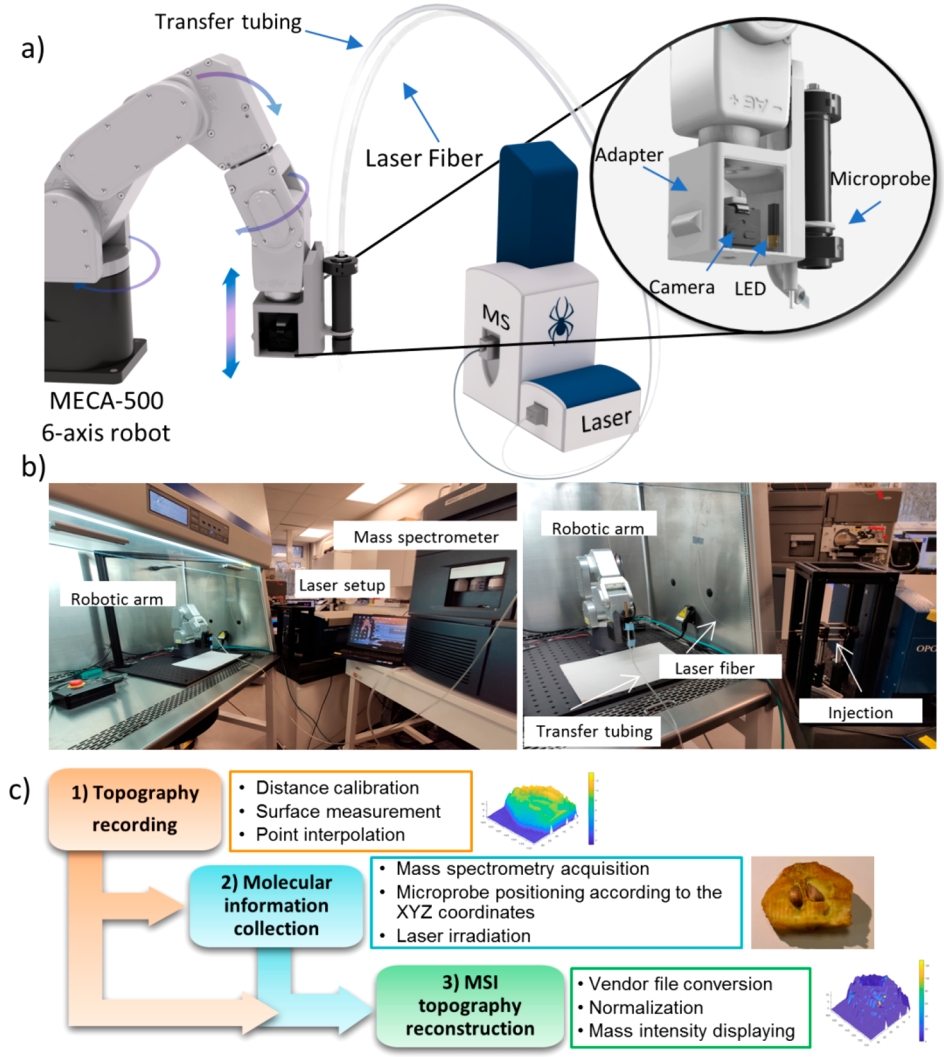

Figure 1. Schematic representation of the Robot-Assisted SpiderMass technology and the general workflow of operation. (a) The SpiderMass probe is attached with an adaptor to the robotic arm. The zoomed part details the distance sensor system with a separate compartment for the camera and an LED laser pointer. The arrows indicate some degrees of movements of the 6-axis robotic arm. (b) Photos of the robot-assisted SpiderMass MSI imaging setup. The layout of the whole system including the robotic arm, laser system and the mass spectrometer (left) and the focus on the robotic arm with the laser fiber and transfer tubing positioned in the fumehood and the laser injection (right). (c) Three-step general workflow of a 3D imaging experiment. First the *x*, *y*, *z* topography is recorded and stored for the correct laser positioning, then the molecular information is collected by a mass spectrometric acquisition, and finally the image is reconstructed and displayed.

endogenous water molecules and provides metabo−lipidomic molecular profiles specific to different cell phenotypes.[11] One of the major advantages of the SpiderMass is the ability to manually move the probe and freely scan any surface without constraint or contact to the specimen.

The development of a combined system including a robotic arm enables, thus, the automated fine motion with the requested precision of the laser microprobe above the sample surface. We also demonstrate that by integrating a height measurement sensor, a topographic image of the surface can be obtained. With this system, topography MSI can be achieved from biological sample with 400−500 μm spatial resolution and below using oversampling rastering.

MATERIAL AND METHODS

Samples. Lipid standard were purchased by Avanti Polar Lipid, U.S.A. Fresh- frozen Wistar rat brains were provided by the biology laboratory, University of Lille. The fresh-frozen brain was sectioned into coronal 12 μm sections using a microtome (Leica Biosystems, Wetzlar, Germany). The sponge (Spontex) piece and apple (Pink Lady) was purchased at the supermarket (Auchan, France). Fresh human abdominal skin discs (12 mm diameter) were purchased from BIOPREDIC International, France. A 3−4-month negative C3(1)/SV40 T-antigen heterozygote transgenic mouse was used for post-mortem imaging right after being sacrificed (see Ethics, Supporting Information (SI)).

Experimental Design. The basic design of the SpiderMass instrument setup is described in detail elsewhere.[7,8] The SpiderMass microprobe was coupled to a commercially available stiff 6D-axis precision MECA robotic arm (MECA-DEMIC, Montreal, Canada) with repeatability of 5 μm, unmatched position and less than 100 μm path accuracy in the *x*, *y*, and *z* dimensions. The SpiderMass handpiece is attached to the robotic arm by a "home-made" 3D printed adaptor equipped with distance sensor, including a camera and LED, for z-hight calibration. The robotic-arm and the SpiderMass

https://doi.org/10.1021/acs.analchem.1c01692
Anal. Chem. 2021, 93, 14383−14391

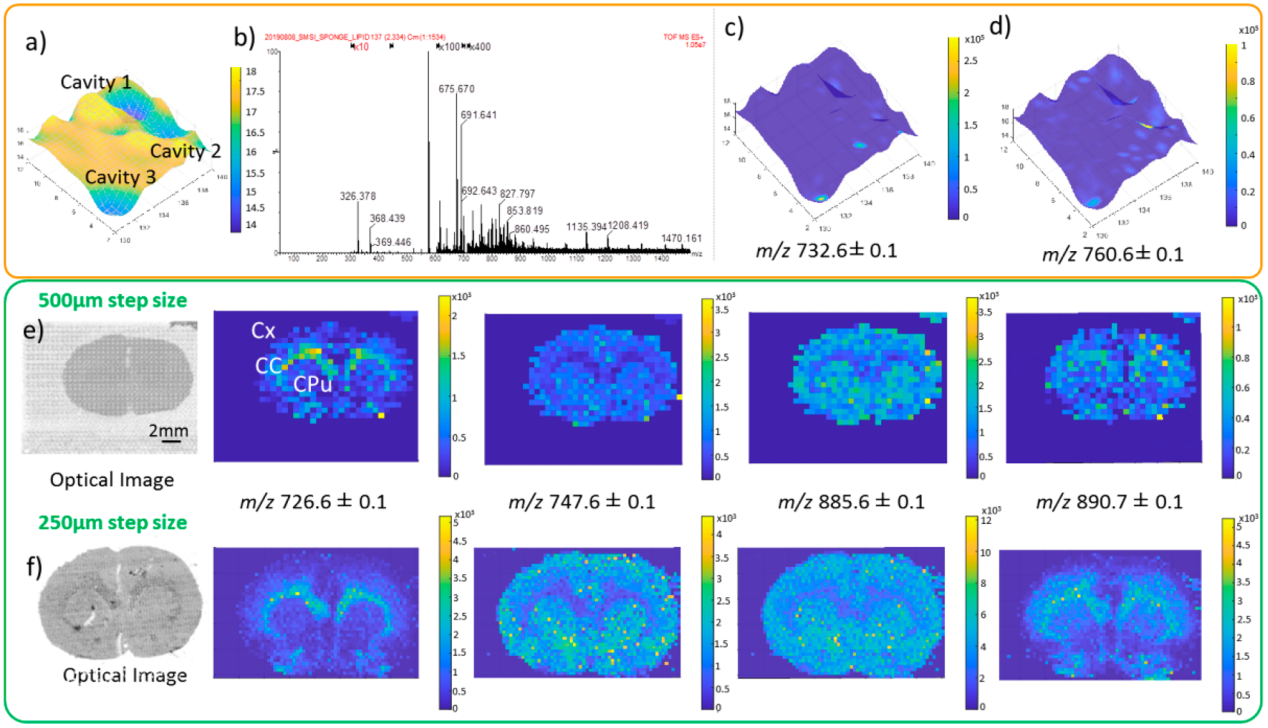

Figure 2. Topography MSI on a sponge with cavities and rat brain tissue section. (A) Topographical 1 cm^2 mesh of the sponge with cavities and color bar indicating changes in height. (B) Mass spectrum obtained from the sponge surface. (C) and (D) Plotted m/z values in positive ion mode with normalized intensities (732.6 ± 0.1 and 760.6 ± 0.1). 2D images of the rat brain with (E) 500 μm step size and (F) 250 μm step size..The ion images correspond to m/z 726.6 ± 0.1 PE (18:1/18:1)-H]-, 747.6 ± 0.1 [PA (22:6/18:0)-H]-, m/z 862.6 ± 0.1 SHexCer 18:1;2_22:0/ [PC(P-18:0_22:1))+Cl]$^-$, m/z 885.7 ± 0.1 [PI(18:0/20:4)-H]-, and m/z 890.7 ± 0.1 SHexCer d18:1/24:0/[PC(O-42:2))+Cl]- (b–f) with TIC normalized intensities.. Abbreviations: Cx, cerebral cortex; CC, corpus callosum; CPU, caudate putamen.

acquisition is controlled by the Matlab (MATLAB inc.) coded framework (SI Figure S1). Several parameters were input such as the height threshold, step size, x and y scanning zone area, and surface threshold. To generate the topographical map, the distance sensor scanned the entire x and y field and registered all of the z-height differences. The x,y,z coordinates were exported as mesh to map for topographical visualization. The SpiderMass probe followed the same x,y,z topographical coordinates as registered in the scan. A detailed description of hardware adjustments, distance sensor, and the automatized interface is provided in the SI.

SpiderMass Acquisition. The acquisition sequence was composed of three consecutive laser shots and 3 s between each step. The laser bursts were automatically fired by the MATLAB user interface. The data was acquired in positive and negative, sensitivity ion mode on the Xevo (G2-S, Q-TOF, Waters, Manchester, UK) mass analyzer through the REIMS prototype interface with biocompatible Tygon tubing. The mass spectrometer acquisition was triggered manually prior to SpiderMass acquisition. MS/MS spectra were recorded with a transfer collision energy range between 25 and 40 V, depending on the selected precursor ion. The lipid annotations were performed manually through LIPIDMAPS database, Alex123 and METLIN database and the lipid assignment was realized with LIPIDMAPS and the literature.[12,13]

Image Processing. A second Matlab code was developed for topographical image coregistration. Small topographical artifacts in the generated mesh were manually removed or averaged.[14] The raw mass spectrometry data was converted into mzXML file using an open source MS converter GUI.[15] Several parameters such as the threshold of the chromatographic peak, the final time of acquisition, mass limits and height threshold were manually set. The selected mass limits were displayed on the topographical image. The absolute intensities of the mass spectrum were selected only from the local maximum of each chromatographic peak. The coregistered images were normalized to the TIC.

RESULTS

Topography MSI Design and Setup. The system was setup with the perspective to realize *in vivo* MSI in humans in the future. The careful design and developments were executed in three different modules including (i) hardware adjustments, (ii) an automatized user interface, and (iii) image reconstruction. The hardware is presented in Figure 1. It includes a 6-axis robotic arm with 5 μm repeatability and 100 μm path accuracy, and an adaptor equipped with a LED and a camera cooperating as a distance sensor. The SpiderMass microprobe is mounted on the arm through the adaptor, including the laser fiber and the transfer line connected to the MS instrument (Figure 1a,b). The zoom into the adaptor specifies the placement of the camera and the LED. The arrows indicate the possible motions of the motors. The photos of the real system setup are shown in Figure 1b. The general workflow of a 3D imaging experiment includes three steps: (1) the topography recording, (2) collection of the molecular data, and (3) the image reconstruction (Figure 1c). First, to start the acquisition, the distance sensor is calibrated by measuring the distance between the LED and the center of the observed camera field (SI Figure S2). Then the investigated specimen is placed under the arm and the (X, Y, Z) coordinates are recorded point

https://doi.org/10.1021/acs.analchem.1c01692
Anal. Chem. 2021, 93, 14383−14391

by point of the defined imaging area at the desired step size to create the topographical map.

To accelerate this step, the resolution of the map can be lowered to reduce the number of collected data points. An interpolation is used to reconstruct the surface at required spatial resolution and stored. Second, the topography is used to correctly position the laser probe. Molecular information is collected at each data point by the mass spectrometer. In the new setup, the topographical and molecular data can be collected at the same time in real-time. Finally, the m/z values of interest are selected, and the images are reconstructed and displayed. The speed of analysis is dependent on the number of laser shots fired at the pixel position, waiting time, and step size. The TIC intensities should reach at least $1e^5$ intensities for good signal reproducibility. With the optimal setup of parameters, an area of 1.5 × 1.5 mm, 16 pixels, TIC $10e^5$, 3 laser shots, 0.5 μm can be imaged in 25 s.

Topographical MSI of Model Samples. We tested the automated robotic arm on several model objects and biological samples starting with the topography imaging step. To determine the accuracy of the z-height profiles we created three topographical maps of a mussel and calculated the z-height average, standard deviation, and coefficient of variance (CV) of five points with the same x,y coordinates. The results are shown in SI Figure S2. The standard deviation resulted in <0.4 and the CV resulted in <0.1 for all selected points displaying high accuracy of the topographical measurements. Examples of topographical maps indicating the objects native forms are shown in SI Figure S3.

Following the 2-step scanning at 500 μm, the topographical and molecular images were coregistered for the small piece of sponge (Figure 2a–d). The topographical image of the 1 cm^2 area (Figure 2a) shows the z-height difference on the imaged surface to be 4 mm with the deepest z at the cavities. The first cavity is 2 mm in depth as indicated by the topographical image and confirmed by measuring with a ruler (SI Figure S4). The spectra showed good signal intensity with the most predominant peaks from the sponge detected at m/z 372.3, 575.3, and 675.6 (SI Figure S5). Because the composition of the sponge is unknown, a second acquisition was performed on the of the same area with the addition of a 1 mL of a lipid standard mix solution containing $[PC(34:1)+H]^+$ and $[PC(32:1)+H]^+$ inside of the cavities. The total ion current (TIC) chromatogram and first indicative pixels are shown in SI Figure S6. Each chromatographic peak corresponds (red bar) to one pixel on the topographical map. A group of chromatographic peaks (blue bar) represent on line in the topographical image. The absolute intensities of the spectra increased to $1e^7$ after spotting the standards and new signals are observed in the m/z [700–900] range (Figure 2b) including m/z 732.6 ± 0.1 and m/z 760.6 ± 0.1 corresponding to the two lipid standards. These signals were used for the MSI reconstruction and plotted to the topographical image (Figure 3c,d, respectively). As indicated in the images, the highest normalized intensities of the two lipid peaks are originating from within the cavities where the lipid standards were deposited.

The user interface was developed to also enable the acquisition and visualization of 2D images from tissue sections (Figure 2). The 2D-imaging mode was tested on a rat brain histological tissue section. First, a virtual topographical image was created with indicated dimensions, and then the MSI acquisition was conducted following the same pattern in the

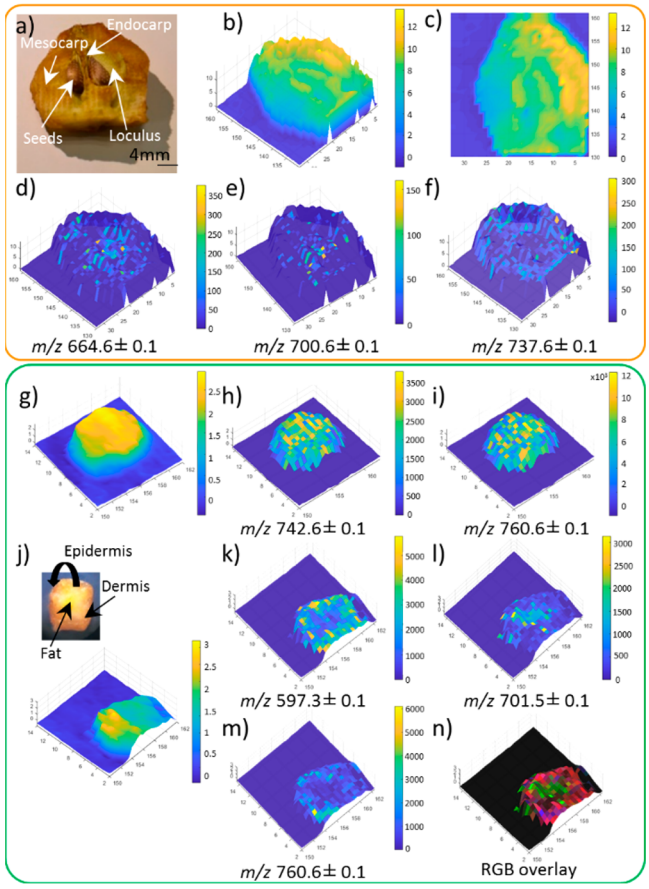

Figure 3. Topography MSI of the apple core with seeds (a)–(f) and fresh skin disc biopsy (g)–(n). (a) The optical image of the apple cross-section with different regions. The 3D topographical map of the apple core in 3D (b) and 2D mode (c) with color bars expressing different heights. The plotted m/z values (d) m/z 664.6 ± 0.1, (e) m/z 700.6 ± 0.1, and (f) m/z 737.6 ± 0.1. Topographical images and an optical image of the fresh skin biopsy acquired from the (g) top and (j) bottom with annotated regions. (h)–(i) Selected ion images and RGB overlay from the skin biopsy acquired from the top at m/z 742.6 ± 0.1 and m/z 760.6 ± 0.1. and (k)–(n) on the bottom at m/z 597.3 ± 0.1 red, m/z 701.6 ± 0.1 green, and m/z 760.6 ± 0.1 blue. All the selected ion images were normalized to the TIC.

negative ion mode (Figure 2e,f, optical images) at 500 μm and with oversampling with 250 μm step size. The acquired TIC mass spectrum in the negative ion mode is shown in SI Figure S7. Some of the most prominent peaks in the lipid m/z [700–1000] range were further selected for coregistration of the molecular images.; m/z 726.6 ± 0.1[PE (18:1_18:1)-H]$^-$, 747.6 ± 0.1 [PA (22:6_18:0)-H]$^-$, m/z 862.6 ± 0.1 SHexCer 18:1;2/22:0/ [PC(P-18:0_22:1))+Cl]$^-$, m/z 885.6 ± 0.1 [PI(18:0_20:4)-H]$^-$, and m/z 890.7 ± 0.1 SHexCer d18:1/24:0, respectively (Figure 3e,f). The images reveal a clear depiction of the white and gray matter in the rat brain tissue, already previously identified.[16,17] Particularly, the images collected at 250 μm revealed improved spatial resolution images and more clearly depicted the Corpus Callosum (CC), Cx–cerebral cortex (Cx), and caudate putamen (CPU). The MS/MS identification of the lipid species can be found in SI Table S1.

3D Topographical Molecular Imaging of Biological Specimens. We further investigated 3D topography MSI by analyzing several biological specimens. In the first example,

https://doi.org/10.1021/acs.analchem.1c01692
Anal. Chem. 2021, 93, 14383–14391

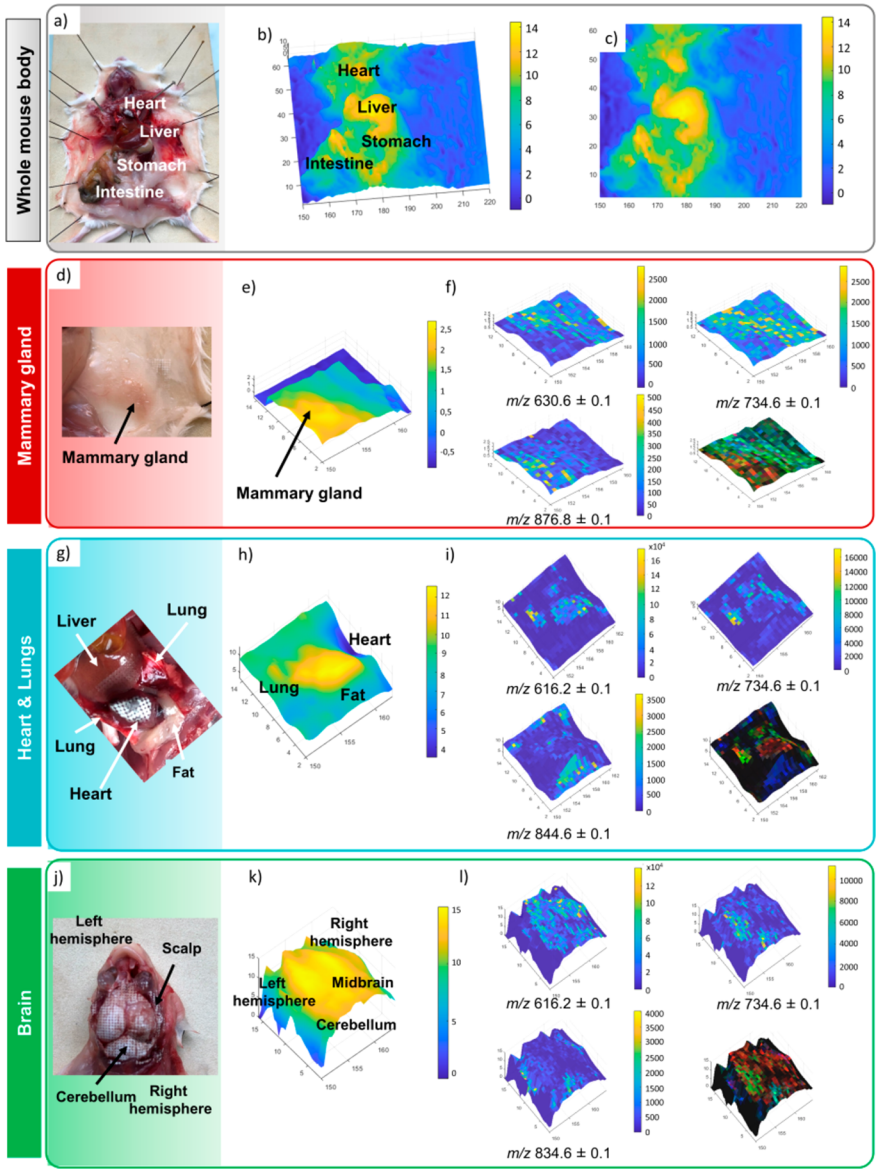

Figure 4. Post-mortem mouse imaging experiments. Optical images of the (a) whole mouse and selected imaging zones; (d) mammary gland, (g) heart and lungs, and (j) brain. Topographical images of the whole mouse in the (b) 3D view, and (c) 2D view. Topographical images of the selected zones depicting different organs and subregions; (e) mammary gland (h) heart and lungs, and (k) brain. The color bars indicate the different topographical heights within the imaged area. (f) selected ion images and RGB overlay for reconstruction red m/z 876.8; green m/z 734.6, blue m/z 630.6 of the mammary gland. (i) selected ion images and RGB overlay for reconstruction red m/z 616.2; green m/z 734.6, blue m/z 844.6 of heart and lungs. (l) selected ion images and RGB overlay for reconstruction red m/z 616.2; green m/z 734.6, blue m/z 834.6 of the brain.

topography MSI was conducted on an apple core with seeds (Figure 3, upper panel). The apple cross-section consists of the mesocarp, endocarp, seeds and loculus region (Figure 3a). The 3D and 2D topographical maps are shown in Figure 3b,c, respectively. The mesocarp, endocarp, and seeds show higher topography than the loculus region. Several ions were reconstructed on the 3D map (Figure 3d–f). Specific ions such as m/z 664.6 ± 0.1 and m/z 700.6 ± 0.1 were more abundant in the seeds and endocarp, whereas m/z 737.6 ± 0.1 was more abundant in the mesocarp. The putative IDs can be found in SI Table S2. Second, we imaged a fresh abdominal skin biopsy (Figure 3, bottom panel). The skin biopsy is composed of the epidermis, dermis, and fatty tissue. Since all different layers cannot be imaged in a single experiment, we conducted experiments first from the top (Figure 3g) and then bottom (Figure 3j) of the biopsy. The epidermis layer is relatively homogeneous; hence no spatial molecular differences were observed as corroborated by the distribution of two ions at m/z 742.6 ± 0.1 (Figure 3h) and m/z 760.6 ± 0.1 (Figure 3i). In contrast, clear molecular differences were observed between the dermis and the fatty tissue (Figure 3k–n). The distribution of the ions at m/z 597.3 ± 0.1 and m/z 760.6 ± 0.1 is mainly found in the dermis region (Figure 3e), whereas the m/z 701.6 ± 0.1 is mainly distributed in the fat (Figure 3f). The RGB overlay of the selected ions is displayed in Figure 3n (red, m/z 597.3 ± 0.1; green, m/z 701.6 ± 0.1, and blue, m/z 760.6 ± 0.1). The MS^2 identification of the lipid species can be found in SI Table S3.

Post-Mortem Imaging Inside of the Body of a Mouse. To explore the outmost potential of the technique, we conducted experiments inside of the whole body of a freshly sacrificed mouse. The whole-body mouse optical and topo-

https://doi.org/10.1021/acs.analchem.1c01692
Anal. Chem. 2021, 93, 14383−14391

graphical images are shown in Figure 4a−c. The images clearly depict different organs such as the intestine, stomach, liver, lungs, and heart. For molecular corelation, several smaller areas were imaged including the mammary gland, the heart and the lungs, and brain (Figure 4d,g,j). The collection of topographical images and molecular data are shown in SI Video 1. The first sequence displays the robotic arm setup and the acquisition of the topographical image of the mammary gland. The SpiderMass probe followed the topographical pattern in sequence two. The third sequence depicts the collection of the molecular data from the brain. The video clearly shows the SpiderMass laser spot size (500 μm) and the path of the microprobe following the topographical image. Figure 4e-f depicts the topographical and molecular images of the mammary gland. While the topographical image reveals only slight differences (2.5 mm, Figure 4e) between the mammary gland and the subcutaneous tissue we can clearly distinguish them molecularly (Figure 4f) Several ions, such as m/z 630.6 ± 0.1 and m/z 734.6 ± 0.1 [PC (32:0) + H]+ show higher abundance in subcutaneous tissue, while the ion m/z 876.8 ± 0.1 is present mainly in the mammary gland. This is even further exemplified by the RGB overlay. In addition, the positive ion mode spectra of the mouse imaging data sets (Figure 4a mammary gland, Figure 4b heart and lungs, and Figure 4c brain) show good sensitivity (in the range 1.0×10^6 at the 600−1500 mass range) with hundreds of different lipid species observed. In the more complex region, such as the heart, we notice greater topographical differences Figure 4h. The selected ions were plotted back to the topographical image in Figure 4i. For example, ion m/z 616.2 ± 0.1 corresponding to heme and most probably associated with hemoglobin is distributed mainly in the heart and lungs, while m/z 734.6 ± 0.1 $[PC (32:0) + H]^+$ is mainly distributed in the lung and surrounding area of the heart. Ions, such as m/z 844.6 ± 0, depict the fatty connective tissue surrounding the heart. These tissue specific differences are even more pronounced in the RGB overlay image. In the last example, the brain images (Figure 4j,k,l) reveal the expected structure separating the right and the left hemisphere. Some detailed topography of the scalp, midbrain, cerebellum is also found in Figure 4k. Selected ions are shown in Figure 4l. The pronounced heme ion at m/z 616.2 ± 0.1 shows the distribution across the whole brain imaged area. This is also consolidated by the optical image displaying the imaged zone Figure 4j. The ion m/z 734.6 ± 0.1 corresponding to $[PC (32:0) + H]^+$ is mainly distributed in the left hemisphere and the cerebellum. This is of no surprise since the particular lipid specie has been repeatedly found in the gray matter of the brain. Although we would expect the distribution of this ion to be the same in the right hemisphere there appears to be a slight difference. This can also be observed in the optical image (Figure 4j), where a part of the right hemisphere does not appear to be imaged probably because of the dissection when the skull was opened. A unique distribution is unravelled by the m/z 834.6 ± 0.1 $[PC (40:6)+H]^+$ of the surrounding scalp and cerebellum. The RGB overlay depicts the exact features of the brain as shown in the optical image. The MS/MS identification of the heme and selected lipid species can be found in SI Table S4. Further multivariate statistical analysis of the imaging data (Figure 5d)) revealed tissue specific discrimination between the brain, heart, and lungs, as well as the discrimination between the mammary gland and subcutaneous tissue (LD3) from the same imaging

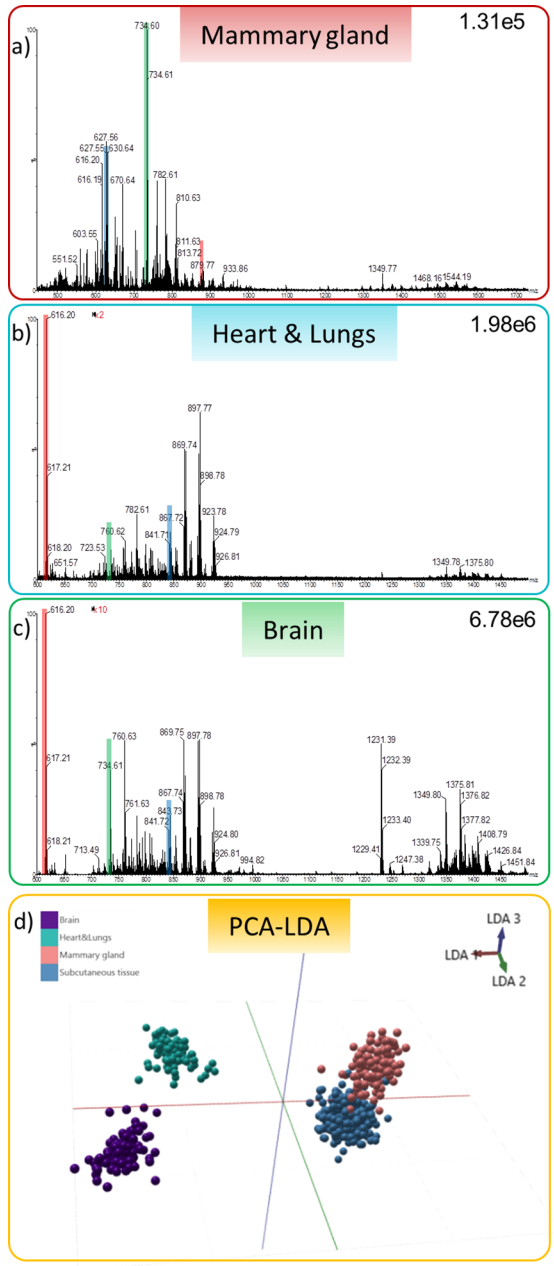

Figure 5. Mass spectra of selected organs from mouse imaging experiments. The representative positive ion mode spectra of (a) mammary gland, (b) heart and lungs, and (c) brain. The color bars indicate the selected ions for molecular image reconstruction and RGB overlays. The spectra are scaled to the highest peak of the selected mass range. (d) PCA-LDA plot of the imaging data contributing to the descrimination of brain, heart and lungs, mammary glands, and subcutaneous tissue.

data set. The discriminative peaks are displayed in the loading plots in SI Figure S8.

***In Vivo* 3D Topography MSI.** Painless topography MSI was also performed *in vivo* on a volunteer finger (Figure 6) and inside of a mussel (SI Figure S9). The topographical and selected ion images well displayed the nail plate, cuticle, and the skin/epidermis layer (Figure 6a). Most of the molecular ions were detected in the epidermis layer, nail folds, and cuticle as shown in m/z 411.3 ± 0.1 and m/z 803.6 ± 0.1 (Figure 6c,e). The ion image m/z 505.3 ± 0.1 (Figure 6d) was the only

https://doi.org/10.1021/acs.analchem.1c01692
Anal. Chem. 2021, 93, 14383−14391

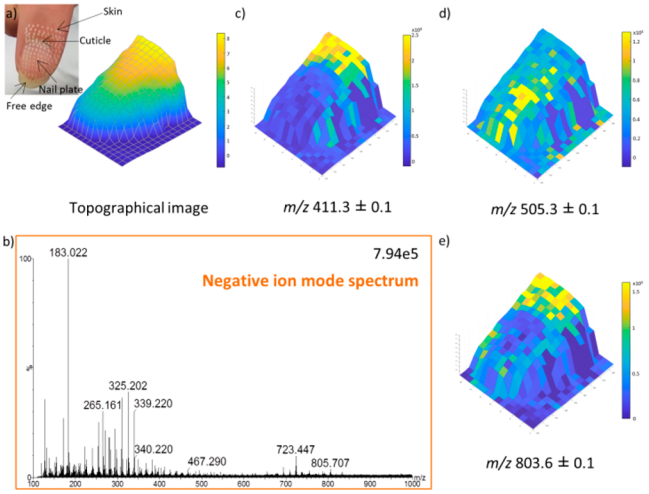

Figure 6. *In vivo* topography MSI of the nail plate, cuticle and skin. (A) An optical and topographical image at 1 mm step. (B) Negative ion mode spectrum. Selected ion images images. (C) m/z 411.3 ± 0.1. (D) m/z 505.3 ± 0.1. (E) m/z 803.6 ± 0.1. All ion images were normalized to the TIC.

image displaying the distribution on the nail plate. The nail plate consists of a protective α-keratin protein with no access water to aid the absorption and ionization process. Therefore, the detection of numerous ions is highly unlikely. The dehydration white trace after analysis was removed by applying water. While the exterior of the mussel also consists of protective, hard material, the inner part of the mussel offers a unique display of organs ideal for *in vivo* analysis. The mussel consists of the posterior, dorsal, ventral, and anterior part each with specific organs (SI Figure S9a,b). The imaged zone and the topographical image are shown SI Figure S9a,c. The selected ion images are attributed to the gills, foot, stomach, and genital papillae of the mussel (SI Figure S9d–g). Particularly, the ion m/z 683.6 ± 0.1 shows a high intensity in the labial palp (SI Figure S9f). Further PCA-LDA (SI Figure S9h) analysis revealed region-specific discrimination between the anterior, ventral, and dorsal part of the mussel. The LDA loading plots and discriminative m/z ions are shown in SI Figure S10.

DISCUSSION

Here, we demonstrate the foundation for the development of *in vivo* real time topographical molecular imaging. We have successfully coupled the SpiderMass to a stiff 6-axis robotic arm and for the first time demonstrate the possibility to conduct MS imaging by moving the probe through the assistance of a robotic arm and coregister the molecular information directly on the topographical image matrix pixel by pixel. Very few MS devices have been coupled to robotic or automated systems. For example, robotic surface analysis using a needle sampling probe attached to the robotic arm was previously described.[14] Using a 3D laser scanner, Li et al. created the 3D images of an object surface and analyzed single spots (0.2 mm × 1.0 mm × 0.6 mm) on the surface by MS using the robotic controlled injection in an open port sampling interface. The molecular information on the analyzed spots was than plotted back to the 3D image but no pixel by pixel coregistration was obtained during the experiments. Collection and data registration are the most crucial parts of imaging experiments. Image fusion is the most common form of coregistration of MSI images in a multimodal approach.[18−21] Here, we plot the distribution of intensities at selected m/z directly on the topographical images via user defined software. Through interpolation, the real-time topographical scanning can be achieved within minutes. With the optimized parameters and the new simultaneous collection of topographical and molecular imaging, we can reach the speed of 1.7 pixels/s at 500 μm step size which is crucial for clinical applications. Therefore, an area of 25 cm^2 can be imaged in roughly 6 min. The current images were acquired at 400−500 μm resolution to demonstrate the potential of the technique. In the future, we plan to adapt the system to create higher spatial resolution images (~100 μm). This could be achieved by new lenses in the hand-held device or by oversampling. The latter attempt already improved the spatial resolution to 250 μm. However, even at the yet used resolution we were able to topographically and molecularly differentiate certain areas of the brain tissue, apple core and seeds, skin punch biopsy, as well as areas within the mussel and mouse body. More concretely, we were able to discriminate specific lipidomic features corresponding to different tissue types of the mammary gland, subcutaneous tissue, heart, lung, and brain. The following examples demonstrate that molecular data can be plotted back onto topographical surfaces of organs bringing molecular knowledge *in vivo* that can be used further for learning or molecular identification. Although the heme ion m/z 616.2 is very evenly distributed in several organs as expected, several lipid species such as $[PC\ (32:0) + H]^+$ at m/z 734.6 were found specific for lung tissue, subcutaneous tissue, and brain tissue. The technology, therefore, clearly demonstrates the ability to discriminate tissue specific features through topographical and molecular images and can be further used to discriminate regions such as resection margins or different cancer subtypes which will help during surgical evaluation.

CONCLUSION AND PERSPECTIVE

We have shown the ability to perform topography MSI in an automated way with the ambition to make the system compatible with the use in the human body. The system is envisioned for future clinical use in oncology surgery as an autonomous device, in contrast to coupling the probe to robot-assisted surgery devices, such as the iKnife and the MasSpec Pen to the Da Vinci robot[22] where the robots still require manual operation by the clinicians. In this way, the automated robot-assisted system will move and screen the desired position indicated by the medical staff and obtained a real-time feedback that could be monitored directly by the medical team though augmented-reality. Some efforts have already been made in this direction by the preliminary in situ analysis.[23] While the available intraoperative hand-held MS devices have proven useful in analysis of numerous cancer tissues, margin delineation and debulking efficiency remain scarce. This remains particularly true with difficult cases where the % of infiltrated cancer cells is low.[24] Incorporating the developed imaging system with deep learning solution would, therefore, leverage and ease the decision-making process during surgery. Taken together, we believe the intended developments and modifications of the modular robot-assisted system will forest the next generation of *in vivo* molecular image guidance used in a surgical room.

https://doi.org/10.1021/acs.analchem.1c01692
Anal. Chem. 2021, 93, 14383−14391

■ ASSOCIATED CONTENT

Supporting Information

The Supporting Information is available free of charge at https://pubs.acs.org/doi/10.1021/acs.analchem.1c01692.

Supplementary experimental procedures, figure of the hardware components, topographical image of the sponge, mass spectrum of the sponge prior to lipid deposition, 3D-robotic topography imaging of the sponge piece, 2D-robotic assisted imaging of a rat brain section and MS/MS lipid fragment tables with identifications (PDF)

Video 1: Topography MSI experiments inside of the body of the freshly sacrificed mouse (MP4)

■ AUTHOR INFORMATION

Corresponding Authors

Isabelle Fournier − *University of Lille, Inserm, CHU Lille, U1192 - Protéomique Réponse Inflammatoire Spectrométrie de Masse − PRISM, F-59000 Lille, France; Institut Universitaire de France (IUF), Paris 75231, France;* orcid.org/0000-0003-1096-5044; Phone: +33 (0)3 20 43 41 94; Email: isabelle.fournier@univ-lille.fr

Christian Duriez − *UMR 9189 - CRIStAL - Centre de Recherche en Informatique, Signal et Automatique de Lille, University of Lille, F-59000 Lille, France*; Phone: +33 (0)3 59 57 78 80; Email: christian.duriez@inria.fr

Authors

Nina Ogrinc − *University of Lille, Inserm, CHU Lille, U1192 - Protéomique Réponse Inflammatoire Spectrométrie de Masse − PRISM, F-59000 Lille, France;* orcid.org/0000-0002-0773-0095

Alexandre Kruszewski − *UMR 9189 - CRIStAL - Centre de Recherche en Informatique, Signal et Automatique de Lille, University of Lille, F-59000 Lille, France*

Paul Chaillou − *UMR 9189 - CRIStAL - Centre de Recherche en Informatique, Signal et Automatique de Lille, University of Lille, F-59000 Lille, France*

Philippe Saudemont − *University of Lille, Inserm, CHU Lille, U1192 - Protéomique Réponse Inflammatoire Spectrométrie de Masse − PRISM, F-59000 Lille, France*

Chann Lagadec − *University of Lille, CNRS, Inserm, CHU Lille, Centre Oscar Lambret, UMR9020 − UMR-S 1277 - Canther − Cancer Heterogeneity, Plasticity and Resistance to Therapies, F-59000 Lille, France*

Michel Salzet − *University of Lille, Inserm, CHU Lille, U1192 - Protéomique Réponse Inflammatoire Spectrométrie de Masse − PRISM, F-59000 Lille, France; Institut Universitaire de France (IUF), Paris 75231, France;* orcid.org/0000-0003-4318-0817

Complete contact information is available at: https://pubs.acs.org/10.1021/acs.analchem.1c01692

Author Contributions

I.F. and N.O. wrote the manuscript original draft; A.K., C.D., I.F., and N.O. designed the experiments. N.O., P.C., and P.S. performed the experiments. C.L. took care of the mice models and assisted for the mouse experiments. I.F., N.O., P.C., and P.S. analyzed the data. A.K., C.D., C.L., I.F., M.S., N.O., P.C., and P.S. corrected the manuscript. C.D., A.K., and C.D. supervised the project. A.K., C.D., I.F., and M.S. provided the funding.

Notes

The authors declare the following competing financial interest(s): I.F. and M.S. are inventors in the SpiderMass patent WO2016046748A1.

■ ACKNOWLEDGMENTS

This work was funded by Ministère de l'Enseignement Supérieur, de la Recherche et de l'Innovation, Université de Lille and Inserm. The project was also funded by ≪Défi Santé numérique≫ joint Inserm/CNRS grant (I.F.) and ISite ULNE (Université Lille Nord-Europe) ERC Generator (I.F.).

■ REFERENCES

(1) Takats, Z.; Strittmatter, N.; McKenzie, J. S. Chapter Nine - Ambient Mass Spectrometry in Cancer Research. In *Adv. Cancer Res.*; Drake, R. R., McDonnell, L. A., Eds.; Applications of Mass Spectrometry Imaging to Cancer; Academic Press, 2017; Vol. *134*, pp 231−256. DOI: 10.1016/bs.acr.2016.11.011.

(2) Zhang, J.; Sans, M.; Garza, K. Y.; Eberlin, L. S. Mass Spectrometry Technologies to Advance Care for Cancer Patients in Clinical and Intraoperative Use *Mass Spectrom. Rev.* **2021***n/a* (n/a). 692.

(3) Vaysse, P.-M.; Heeren, R. M. A.; Porta, T.; Balluff, B. *Analyst* **2017**, *142* (15), 2690−2712.

(4) Balog, J.; Sasi-Szabó, L.; Kinross, J.; Lewis, M. R.; Muirhead, L. J.; Veselkov, K.; Mirnezami, R.; Dezsö, B.; Damjanovich, L.; Darzi, A.; Nicholson, J. K.; Takáts, Z. *Sci. Transl. Med.* **2013**, *5* (194), 194ra93−194ra93.

(5) Balog, J.; Kumar, S.; Alexander, J.; Golf, O.; Huang, J.; Wiggins, T.; Abbassi-Ghadi, N.; Enyedi, A.; Kacska, S.; Kinross, J.; Hanna, G. B.; Nicholson, J. K.; Takats, Z. *Angew. Chem., Int. Ed.* **2015**, *54* (38), 11059−11062.

(6) Manoli, E.; Mason, S.; Ford, L.; Adebesin, A.; Bodai, Z.; Darzi, A.; Kinross, J.; Takats, Z. Validation of Ultrasonic Harmonic Scalpel for Real-Time Tissue Identification Using Rapid Evaporative Ionization Mass Spectrometry *Anal. Chem.* **2021**. *935906*.

(7) Fatou, B.; Saudemont, P.; Leblanc, E.; Vinatier, D.; Mesdag, V.; Wisztorski, M.; Focsa, C.; Salzet, M.; Ziskind, M.; Fournier, I. *Sci. Rep.* **2016**, *6*, 25919.

(8) Ogrinc, N.; Saudemont, P.; Balog, J.; Robin, Y.-M.; Gimeno, J.-P.; Pascal, Q.; Tierny, D.; Takats, Z.; Salzet, M.; Fournier, I. *Nat. Protoc.* **2019**, *14* (11), 3162−3182.

(9) Woolman, M.; Gribble, A.; Bluemke, E.; Zou, J.; Ventura, M.; Bernards, N.; Wu, M.; Ginsberg, H. J.; Das, S.; Vitkin, A.; Zarrine-Afsar, A. Optimized Mass Spectrometry Analysis Workflow with Polarimetric Guidance for Ex Vivo and in Situ Sampling of Biological Tissues *Sci. Rep.* **2017**, *7*. DOI: 10.1038/s41598-017-00272-y.

(10) Zhang, J.; Rector, J.; Lin, J. Q.; Young, J. H.; Sans, M.; Katta, N.; Giese, N.; Yu, W.; Nagi, C.; Suliburk, J.; Liu, J.; Bensussan, A.; DeHoog, R. J.; Garza, K. Y.; Ludolph, B.; Sorace, A. G.; Syed, A.; Zahedivash, A.; Milner, T. E.; Eberlin, L. S. *Sci. Transl. Med.* **2017**, *9* (406), eaan3968.

(11) Saudemont, P.; Quanico, J.; Robin, Y.-M.; Baud, A.; Balog, J.; Fatou, B.; Tierny, D.; Pascal, Q.; Minier, K.; Pottier, M.; Focsa, C.; Ziskind, M.; Takats, Z.; Salzet, M.; Fournier, I. Real-Time Molecular Diagnosis of Tumors Using Water-Assisted Laser Desorption/Ionization Mass Spectrometry Technology *Cancer Cell* **2018**. *34*840.

(12) Pauling, J. K.; Hermansson, M.; Hartler, J.; Christiansen, K.; Gallego, S. F.; Peng, B.; Ahrends, R.; Ejsing, C. S. *PLoS One* **2017**, *12* (11), e0188394.

(13) Smith, C. A.; O'Maille, G.; Want, E. J.; Qin, C.; Trauger, S. A.; Brandon, T. R.; Custodio, D. E.; Abagyan, R.; Siuzdak, G. METLIN: A Metabolite Mass Spectral Database *Ther. Drug Monit.* **2005**, *27*.747

(14) Li, A.; Paine, M. R. L.; Zambrzycki, S.; Stryffeler, R. B.; Wu, J.; Bouza, M.; Huckaby, J.; Chang, C.-Y.; Kumar, M.; Mukhija, P.; Fernández, F. M. *Anal. Chem.* **2018**, *90* (6), 3981−3986.

(15) Chambers, M. C.; Maclean, B.; Burke, R.; Amodei, D.; Ruderman, D. L.; Neumann, S.; Gatto, L.; Fischer, B.; Pratt, B.;

Egertson, J.; Hoff, K.; Kessner, D.; Tasman, N.; Shulman, N.; Frewen, B.; Baker, T. A.; Brusniak, M.-Y.; Paulse, C.; Creasy, D.; Flashner, L.; Kani, K.; Moulding, C.; Seymour, S. L.; Nuwaysir, L. M.; Lefebvre, B.; Kuhlmann, F.; Roark, J.; Rainer, P.; Detlev, S.; Hemenway, T.; Huhmer, A.; Langridge, J.; Connolly, B.; Chadick, T.; Holly, K.; Eckels, J.; Deutsch, E. W.; Moritz, R. L.; Katz, J. E.; Agus, D. B.; MacCoss, M.; Tabb, D. L.; Mallick, P. *Nat. Biotechnol.* **2012**, *30* (10), 918−920.

(16) Zou, J.; Talbot, F.; Tata, A.; Ermini, L.; Franjic, K.; Ventura, M.; Zheng, J.; Ginsberg, H.; Post, M.; Ifa, D. R.; Jaffray, D.; Miller, R. J. D.; Zarrine-Afsar, A. *Anal. Chem.* **2015**, *87* (24), 12071−12079.

(17) Nemes, P.; Woods, A. S.; Vertes, A. *Anal. Chem.* **2010**, *82* (3), 982−988.

(18) Van de Plas, R.; Yang, J.; Spraggins, J.; Caprioli, R. M. *Nat. Methods* **2015**, *12* (4), 366−372.

(19) Vollnhals, F.; Audinot, J.-N.; Wirtz, T.; Mercier-Bonin, M.; Fourquaux, I.; Schroeppel, B.; Kraushaar, U.; Lev-Ram, V.; Ellisman, M. H.; Eswara, S. *Anal. Chem.* **2017**, *89* (20), 10702−10710.

(20) Tarolli, J. G.; Jackson, L. M.; Winograd, N. *J. Am. Soc. Mass Spectrom.* **2014**, *25* (12), 2154−2162.

(21) Abdelmoula, W. M.; Regan, M. S.; Lopez, B. G. C.; Randall, E. C.; Lawler, S.; Mladek, A. C.; Nowicki, M. O.; Marin, B. M.; Agar, J. N.; Swanson, K. R.; Kapur, T.; Sarkaria, J. N.; Wells, W.; Agar, N. Y. R. *Anal. Chem.* **2019**, *91* (9), 6206−6216.

(22) Keating, M. F.; Zhang, J.; Feider, C. L.; Retailleau, S.; Reid, R.; Antaris, A.; Hart, B.; Tan, G.; Milner, T. E.; Miller, K.; Eberlin, L. S. *Anal. Chem.* **2020**, *92* (17), 11535−11542.

(23) Woolman, M.; Qiu, J.; Kuzan-Fischer, C. M.; Ferry, I.; Dara, D.; Katz, L.; Daud, F.; Wu, M.; Ventura, M.; Bernards, N.; Chan, H.; Fricke, I.; Zaidi, M.; Wouters, B. G.; Rutka, J. T.; Das, S.; Irish, J.; Weersink, R.; Ginsberg, H. J.; Jaffray, D. A.; Zarrine-Afsar, A. *Chem. Sci.* **2020**, *11* (33), 8723−8735.

(24) King, M. E.; Zhang, J.; Lin, J. Q.; Garza, K. Y.; DeHoog, R. J.; Feider, C. L.; Bensussan, A.; Sans, M.; Krieger, A.; Badal, S.; Keating, M. F.; Woody, S.; Dhingra, S.; Yu, W.; Pirko, C.; Brahmbhatt, K. A.; Buren, G. V.; Fisher, W. E.; Suliburk, J.; Eberlin, L. S. Rapid Diagnosis and Tumor Margin Assessment during Pancreatic Cancer Surgery with the MasSpec Pen Technology *Proc. Natl. Acad. Sci. U. S. A.* **2021**, *118* (28). e2104411118.

https://doi.org/10.1021/acs.analchem.1c01692
Anal. Chem. 2021, 93, 14383−14391